Received: 22 August 2023 | Revised: 20 November 2023 | Accepted: 23 November 2023 | Published online: 5 December 2023

RESEARCH ARTICLE

Journal of Optics and Photonics Research
2024, Vol. 1(2) 74–81
DOI: 10.47852/bonviewJOPR32021565

BON VIEW PUBLISHING

Dual-Frequency Lidar for Compressed Sensing 3D Imaging Based on All-Phase Fast Fourier Transform

Xiaotian Li[1,2,3], Yetong Hu[1,2,3], Yuchen Jie[1,2,3], Changming Zhao[1,2,3] and Zilong Zhang[1,2,*]

[1]*School of Optics and Photonics, Beijing Institute of Technology, China*

[2]*Key Laboratory of Photoelectronic Imaging Technology and System, Ministry of Education of People's Republic of China, China*

[3]*Key Laboratory of Photonics Information Technology, Ministry of Industry and Information Technology, China*

Abstract: Lidar, with its advantages of high measurement accuracy, fine angular resolution, and strong anti-interference capability, plays a pivotal role in the field of scene depth information acquisition. Traditional approaches to achieving lateral spatial resolution in imaging include raster scanning and array detectors. The former necessitates frequent scanning to acquire depth maps, resulting in time consumption and instability. The latter encounters challenges such as high dark count rates, pixel crosstalk, and excessive costs for obtaining high-resolution images using array detectors. The introduction of compressed sensing (CS) offers a novel perspective on realizing non-scanning three-dimensional imaging. In this context, we propose a novel three-dimensional imaging system that combines CS with coherent dual-frequency continuous-wave lidar and utilizes the all-phase fast Fourier transform to extract both amplitude and phase information. This system requires only M measurements, and through a reconstruction algorithm, it achieves the inversion of depth information for N-pixel scenes ($M << N$). Integrating cost-effective components such as digital micromirrors and single-point detectors, this affordable system accomplishes three-dimensional imaging of a single target. Notably, it significantly reduces the required number of measurements while concurrently ensuring enhanced eye safety and signal-to-noise ratio.

Keywords: compressed sensing, dual-frequency lidar, 3D imaging, all-phase FFT

1. Introduction

Single-pixel imaging (SPI), as an emerging computational imaging approach, involves modulating the target light field through a series of patterns and collecting the data using a single-pixel detector [1–3]. This method significantly reduces the number of measurements while maintaining a high signal-to-noise ratio and a wide operational bandwidth. However, conventional SPI tends to lose the depth information of the target during the acquisition process, resulting in reconstructed images containing only two-dimensional information [4]. To address this limitation and achieve depth acquisition in SPI, numerous methods have been proposed [4–9]. Among them, laser radar stands out for its higher accuracy, improved resolution, and enhanced coherence. In this paper, we place emphasis on introducing a technique that combines compressed sensing (CS) with lidar to realize single-pixel three-dimensional imaging.

CS is already used in pulsed lidar systems, with the majority of research employing image cube-based approaches [10–12]. During measurements, a spatial light modulator loads a mask pattern to capture intensity values at different depth positions within the scene. By correlating the mask pattern with measured light intensities at different depths, two-dimensional images for each depth within the scene are obtained. Consequently, a three-dimensional image cube is constructed from these two-dimensional images. In this regard, one of the most representative studies is the work conducted by Sun et al. [12]. Sun et al. [12] employed pulsed structured illumination and high-speed photodetectors to achieve compressive sensing three-dimensional imaging of targets within a 5-m range. This approach yielded depth and intensity maps of 128 × 128 pixels, with a ranging accuracy of less than 3 mm. Additionally, Sun et al. [12] demonstrated real-time video at a frame rate of 12 Hz using an evolved compressive sensing strategy. However, the inherent speed of light demands the use of detectors with rapid response times and high-speed electronic readout to achieve high-precision depth resolution. This requirement results in increased costs. Furthermore, this method needs to perform CS recovery many times, which consumes a lot of computing resources and time.

The continuous-wave (CW) lidar systems primarily consist of amplitude-modulated continuous wave (AMCW) lidar and frequency-modulated continuous wave (FMCW) lidar. The application of CS to CW lidar systems is still in its nascent

*Corresponding author: Zilong Zhang, School of Optics and Photonics, Beijing Institute of Technology and Key Laboratory of Photoelectronic Imaging Technology and System, Ministry of Education of People's Republic of China, China. Email: zlzhang@bit.edu.cn

Table 1
Comparison of related research on the combination of CS and lidar

Institution	Year	Regime	Experiment	Resolution	Results/Description
University of Rochester [10]	2013	Pulsed	Yes	256 × 256	Distance resolution is about 2.54 cm
Beihang University [12]	2016	Pulsed	Yes	128 × 128	Accuracy less than 3 mm in the range of 5 m
University of Rochester [16]	2018	FMCW	No	128 × 128	The combination of CS and FMCW lidar was first reported
Hangzhou Dianzi University [17]	2020	AMCW	Yes	16 × 16	Poor shape and depth of reconstructed objects
Beijing Institute of Technology [15]	2021	AMCW	No	128 × 128	Stayed in the simulation stage
Beihang University [19]	2022	AMCW	Yes	64 × 64	Depth map and intensity map can be restored at the same time
Wuhan University [11]	2023	Pulsed	Yes	96 × 48	Mainly corrected for photon counting detector dead time and shot noise
Beijing Institute of Technology*	2023	DFL-CW	Yes	32 × 32	Shape contours can be distinguished, with an average distance error of 3.7 cm

*This manuscript

stages, with most research confined to simulation phases [13–19]. Table 1 displays representative works that integrate CS with pulsed or CW lidar. Coherent dual-frequency CW lidar is a detection technology that combines the optical advantages of laser radar with the mature engineering application technology of microwave radar in a CW regime [20]. During the atmospheric transmission process, atmospheric turbulence interferes with laser beams of two frequencies in the same manner. Therefore, the beat frequency signal generated by dual-frequency laser interference can counteract the effects of atmospheric turbulence and backscattering speckle noise during transmission. This feature endows dual-frequency lidar with excellent resistance to atmospheric interference. Coherent dual-frequency lidar has relatively low requirements for the tunability of light sources, extends the detection range, and offers superior distance resolution and ranging accuracy comparable to or even better than pulse-based lidar. Therefore, combining CS with dual-frequency lidar holds great promise for long-range detection.

The observation matrix is a critical factor affecting compressive sensing imaging [21–23]. Given that CS relies on a limited number of measurements, whether through structured illumination or structured detection, the choice of the observation matrix must be made with great care. A well-designed set of patterns allows for better image reconstruction with fewer samples, reducing the time required for sampling the target and minimizing the memory required for storing projection patterns and sampling information. In SPI, the commonly used spatial light modulator is the digital micromirror device (DMD). Utilizing binary Hadamard matrices as masks enables direct utilization of DMD, a high-speed binary spatial light modulator, for SPI. Moreover, Hadamard matrices possess excellent deterministic orthogonality properties, making them suitable for precomputation and storage, thereby enhancing imaging efficiency and reducing storage costs. In recent years, several studies have focused on different orders of Hadamard matrices, such as Walsh orders, Russian doll orders [24], and cake-cutting orders [25]. However, most research on Hadamard matrix orders primarily pertains to two-dimensional compressive sensing imaging, with limited exploration of their performance in the field of three-dimensional imaging.

In this study, we amalgamate coherent dual-frequency CW lidar with CS techniques. After comparing the impact of various modulation matrices on the performance of three-dimensional imaging, we have chosen a "cake cutting" (CC order) strategy as the observation matrix for our method in the compression imaging process. The proposed single-pixel three-dimensional imaging method is validated through theoretical derivations and simulation experiments, showcasing robust ranging accuracy and interference resilience. Finally, an experimental setup is constructed to perform three-dimensional imaging on single targets of varying shapes. The main contributions of this paper are summarized as follows:

(1) This paper combined coherent dual-frequency CW lidar systems with CS, filling the gap in the field of CS for three-dimensional imaging. Compared to pulsed lidar, CW lidar exhibits higher accuracy, lower detector requirements and requires fewer reconstruction computations when combined with CS.
(2) This paper, for the first time, utilized the phase of the signal extracted through all-phase fast Fourier transform in compressive sensing reconstruction. It overcame issues that traditional spectral analysis methods struggled with, such as spectral leakage, effectively improving the accuracy of the reconstructed depth maps.

2. Basic Principle

2.1. Observation matrix

The natural order Hadamard matrix possesses a universal recursive construction formula [25]:

$$H_{2^k} = \begin{bmatrix} H_{2^{k-1}} & H_{2^{k-1}} \\ H_{2^{k-1}} & -H_{2^{k-1}} \end{bmatrix} = H_2 \otimes H_{2^{k-1}} \tag{1}$$

where $H_1 = 1$, 2^k is the order of the Hadamard matrix, with k a non-negative integer greater than or equal to 2, and $\otimes$ represents the Kronecker product.

The Walsh order Hadamard matrices are matrices obtained by rearranging the rows of a natural order Hadamard matrix in

increasing order of the number of changes in binary symbols per row. Transitioning from a natural order Hadamard matrix to a Walsh order Hadamard matrix can also be achieved through methods involving bit-reversal arrangements along with Gray code arrangements.

The Russian doll order is primarily based on the principle that each Hadamard matrix contains scaled-down versions of lower-order Hadamard matrices. A breakdown of the process is as follows: Step One: Rearrange the rows of the Hadamard matrix. The first half of the Hadamard matrix H1 becomes H2, the first quarter becomes H3, the first eighth becomes H4, and so on, with each subsequent section containing a scaled-down version of the previous one. Step Two: Leveraging the symmetry of the Hadamard matrix, divide the masks arranged in the first step into four parts. Rearrange the third part to be the transpose of the second part. Step Three: Define each mask's continuous region that contains identical values as a block. Arrange the masks from the four parts in ascending order based on the number of blocks they contain.

The cake-cutting order Hadamard matrix is obtained by directly rearranging the rows of the natural order Hadamard matrix in increasing order of the number of two-dimensional connected domains in the binary masks based on the natural order Hadamard basis.

2.2. The principle of 3D imaging based on CS

The coherent dual-frequency laser is received and responded to the photoelectric detector, and this can be represented as follows:

$$x_T(t) = P_0\, cos(2\pi ft + \varphi_0) \tag{2}$$

where P_0 is the amplitude of laser intensity, f is the frequency difference of the coherent dual-frequency laser, and φ_0 is the initial phase. To obtain an image of resolution $n \times n$, it is necessary to load the DMD micromirror M times with a measurement matrix of resolution $n \times n$. The signal received by the single-point detector is the sum of echoes corresponding to n^2 pixels. Therefore, the total received echo for the k th measurement is

$$\begin{aligned} x_R^k(t) &= P_R^k\, cos(2\pi ft + \varphi_0 + \Delta\phi^k) \\ &= cos(2\pi ft + \varphi_0) \cdot \left[P_R^k\, cos(\Delta\phi^k)\right] - sin(2\pi ft + \varphi_0) \\ &\quad \cdot \left[P_R^k\, sin(\Delta\phi^k)\right] \\ &= \sum_{i=1}^{n}\sum_{j=1}^{n} c_{ij}^k P_{ij}\, cos(2\pi ft + \varphi_0 + \Delta\varphi_{ij}) \\ &= \sum_{i=1}^{n}\sum_{j=1}^{n} c_{ij}^k P_{ij}[\, cos(2\pi ft + \varphi_0)\, cos(\Delta\varphi_{ij}) \\ &\quad - sin(2\pi ft + \varphi_0) sin(\Delta\varphi_{ij})] \\ &= cos(2\pi ft + \varphi_0) \cdot \sum_{i=1}^{n}\sum_{j=1}^{n} c_{ij}^k P_{ij}\, cos(\Delta\varphi_{ij}) \\ &\quad - sin(2\pi ft + \varphi_0) \cdot \sum_{i=1}^{n}\sum_{j=1}^{n} c_{ij}^k P_{ij}\, sin(\Delta\varphi_{ij}) \end{aligned} \tag{3}$$

where $P_R^k, \Delta\phi^k$ represents the amplitude and phase of the actual response signal from the photoelectric detector for the k th measurement, $\Delta\varphi_{ij}$ is the additional phase difference generated at the i th row and j th column pixel of the scene due to varying distances from the detector, P_{ij} is the corresponding amplitude at that position, and c_{ij} is the state of the individual micromirror at that position when different observation matrices are loaded onto the DMD.

$$c_{ij} = \begin{cases} 0 \\ 1 \end{cases} \tag{4}$$

According to the corresponding relationship, it can be obtained:

$$\begin{cases} \sum_{i=1}^{n}\sum_{j=1}^{n} c_{ij}^k P_{ij}\, cos(\Delta\varphi_{ij}) = P_R^k\, cos(\Delta\phi^k) = a^k \\ \sum_{i=1}^{n}\sum_{j=1}^{n} c_{ij}^k P_{ij}\, sin(\Delta\varphi_{ij}) = P_R^k\, sin(\Delta\phi^k) = b^k \end{cases} \tag{5}$$

After M measurements, two sets of measurement values A and B can be obtained:

$$\begin{aligned} A = CX_1 = [a^1, a^2, \cdots, a^k, \cdots a^M]^T \\ B = CX_2 = [b^1, b^2, \cdots, b^k, \cdots b^M]^T \end{aligned} \tag{6}$$

Among them, C is the observation matrix, and X_1 and are X_2 combinations of amplitude values and phase values of sine and cosine at each pixel position:

$$C = \begin{bmatrix} c_{11}^1 & c_{12}^1 & \cdots & c_{1n}^1 & \cdots & c_{n1}^1 & \cdots & c_{nn-1}^1 & c_{nn}^1 \\ \vdots & \vdots & \ddots & \vdots & \ddots & \vdots & \ddots & \vdots & \vdots \\ c_{11}^k & c_{12}^k & \cdots & c_{1n}^k & \cdots & c_{n1}^k & \cdots & c_{nn-1}^k & c_{nn}^k \\ \vdots & \vdots & \ddots & \vdots & \ddots & \vdots & \ddots & \vdots & \vdots \\ c_{11}^{M-1} & c_{12}^{M-1} & \cdots & c_{1n}^{M-1} & \cdots & c_{n1}^{M-1} & \cdots & c_{nn-1}^{M-1} & c_{nn}^{M-1} \\ c_{11}^M & c_{12}^M & \cdots & c_{1n}^M & \cdots & c_{n1}^M & \cdots & c_{nn-1}^M & c_{nn}^M \end{bmatrix} \tag{7}$$

$$\begin{aligned} X_1 &= [\, P_{11}\, cos\Delta\varphi_{11} \cdots P_{1n}\, cos\Delta\varphi_{1n} \ \cdots \ P_{n1}\, cos\Delta\varphi_{n1} \cdots P_{nn}\, cos\Delta\varphi_{nn} \,] \\ X_2 &= [\, P_{11}\, sin\Delta\varphi_{11} \cdots P_{1n}\, sin\Delta\varphi_{1n} \ \cdots \ P_{n1}\, sin\Delta\varphi_{n1} \cdots P_{nn}\, sin\Delta\varphi_{nn} \,] \end{aligned} \tag{8}$$

The observation matrix and observation values are input into the TVAL3 solver to obtain the optimal solution through two iterations of solving. It is clearly evident that the phase information of echo from different pixels in a two-dimensional scene and the distance to the distance detector can be obtained using Equation (8).

$$\begin{cases} \Delta\Phi = arctan\dfrac{X_2}{X_1} \\ d = \dfrac{c}{4\pi f}\Delta\Phi \end{cases} \tag{9}$$

3. Simulation Experiments

3.1. All-phase FFT

As mentioned in Equation (5) in the previous section, the three-dimensional compression imaging method proposed in this paper requires the extraction of both the magnitude and phase of coherent dual-frequency laser echo signals. However, due to challenges such as spectral leakage and the Gibbs phenomenon faced by the discrete Fourier transform, improper CS observations can arise, severely impacting the accuracy of depth map recovery. To address this issue, the present study employs the all-phase fast Fourier transform (APFFT) algorithm for correcting the amplitude and phase of the echo signals collected from the detector. The

APFFT algorithm consists of two components: full-phase preprocessing of the input sequence and fast Fourier transform (FFT) analysis of the processed data.

Assuming a uniform rectangular window as the applied window function, the processing is conducted on the time-domain signal $x(t)$ with frequency f_0 and sampling frequency f_s. The outputs of FFT and APFFT are illustrated in Equations (10) and (11) respectively [20]:

$$X_N(k) = A\frac{sin(\pi(k-m))}{sin(\pi(k-m)/N)}e^{j[(1-N)(k-m)\pi/N+\varphi_0]} \quad k = 0, 1, \ldots, N-1 \tag{10}$$

$$X_N(k) = A\frac{sin^2(\pi(m-k))}{sin^2(\pi(m-k)/N)}e^{j\varphi_0} \quad k = 0, 1, \ldots, N-1 \tag{11}$$

Here, A represents the amplitude, N is the signal length, φ_0 signifies the initial phase, and m is defined as $m = N \times \frac{f_0}{f_s}$.

Comparing Equations (10) and (11), concerning the amplitude characteristic, the APFFT spectral amplitude of signal $x(t)$ for all spectral lines is the square of the traditional FFT spectral amplitude. This quadratic attenuation relationship is applied to both sidelobes and main lobes, making the main spectral lines more prominent. Thus, APFFT exhibits a significant ability to suppress spectral leakage. Regarding the phase characteristic, after undergoing APFFT, the phase value of the spectral lines remains constant at the phase value of the central sample point, independent of frequency offset. This grants APFFT phase invariance, eliminating the need for spectrum correction as required by conventional FFT methods.

To validate the corrective capability of the all-phase fast Fourier transform, the following computer simulation experiment is conducted: with a signal frequency of 10 MHz and a signal length of 2048 points, sampling frequencies ranging from 100 MHz to 1 GHz are considered. For each sampling frequency, 100 sets of randomly generated sinusoidal signals with random amplitude and phase are processed using both traditional FFT and all-phase FFT transforms (both with applied Hanning window). The average amplitude error and phase error are recorded for comparison. Simulation results are depicted in Figure 1. The results show that the average amplitude error of APFFT is controlled within 0.0017, the average phase error is controlled within 6×10^{-10}, and the performance is far superior to the traditional FFT algorithm, which can be used as a signal processing algorithm in the three-dimensional compression imaging system proposed in this paper.

3.2. 3D imaging

To validate the feasibility of the compressive sensing three-dimensional imaging system based on coherent dual-frequency laser radar, the following simulation experiment is designed.

A single-frequency seed source with a wavelength of 1064 nm is utilized, and a dual-frequency laser with a frequency difference of 10 MHz is obtained through electro-optic modulation. The targets consist of the letter "C" positioned 5 m away from the laser emission end and the letter "S" located 10 m away. The echoes reflected from the targets are modulated by a DMD, which loads the Hadamard matrices with different permutation orders as the observation matrices. The final optical signal is collected by a single-pixel detector. In the simulation experiment, a sampling frequency of 1 GHz and 2048 sampling points are employed. The signal processing algorithm is APFFT, and the compressive sensing recovery algorithm employs the TVAL3 solver. This setup ultimately achieves compressive sensing depth imaging at a resolution of 64 × 64 under various compression ratios. The evaluation of the reconstruction quality is judiciously carried out using the root mean square error (RMSE) metric. It is important to note that a lower RMSE value signifies a higher quality of reconstruction, with RMSE values approaching 0 indicative of exceptional performance.

Figure 2(a)–(e) depicts the patterns of 16th-order Hadamard matrices corresponding to different ordering strategies, including natural order, Walsh order, random order, cake-cutting order, and Russian doll order. Figure 2(f) illustrates the impact of Hadamard matrices with different ordering strategies on the performance of a dual-frequency laser compressive sensing system for three-dimensional imaging at various compression ratios. Simulation results indicate that all five ordering strategies exhibit excellent recovery performance at high compression ratios. However, at lower compression ratios, the natural order performs the least effectively. Notably, the cake-cutting order demonstrates impressive recovery performance under both low and high compression ratios. Consequently, we have chosen the cake-cutting order as the observation matrix for this paper's compressive sensing approach.

After selecting the cake-cutting order Hadamard matrix as the observation matrix, we conducted compressive sensing three-dimensional imaging on the simulated targets mentioned earlier. We chose a low sampling rate with compression ratios ranging from 5% to 15%. The reconstructed depth maps are presented in Figure 3(a). The proposed 3D compression imaging method demonstrates its remarkable efficiency by requiring only a limited number of measurements for the reconstruction of depth maps.

Figure 1

(a) Average amplitude error of APFFT and FFT at different sampling rates. (b) Average phase error of APFFT and FFT at different sampling rates

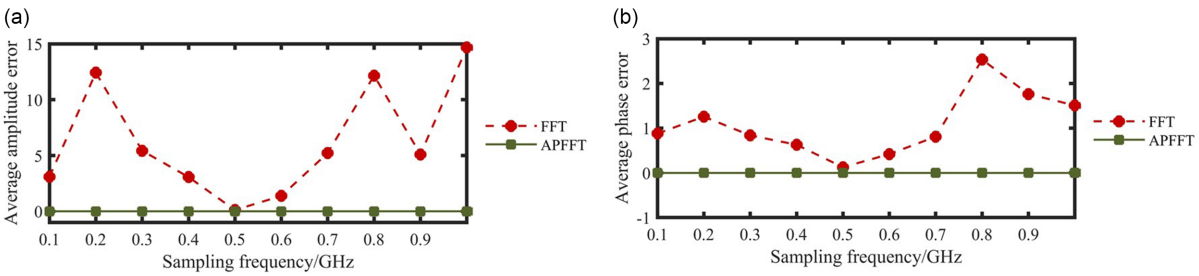

Figure 2
A comparison of various ordering strategies and their impact on three-dimensional imaging in a dual-frequency laser compressed sensing system. (a) Natural order. (b) Walsh order. (c) Random order. (d) Cake-cutting order. (e) Russian doll order. (f) Simulation results of different sorting strategies

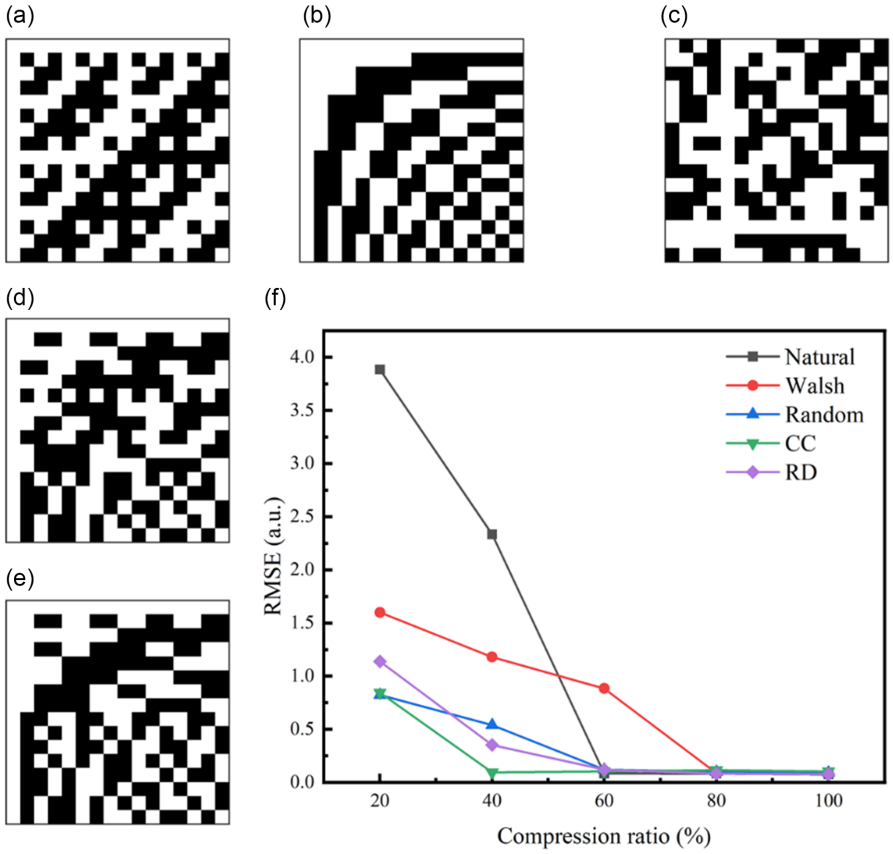

Figure 3
Reconstructed depth maps under different compression ratios. (a) No noise. (b) Adding 10 dB Gaussian white noise

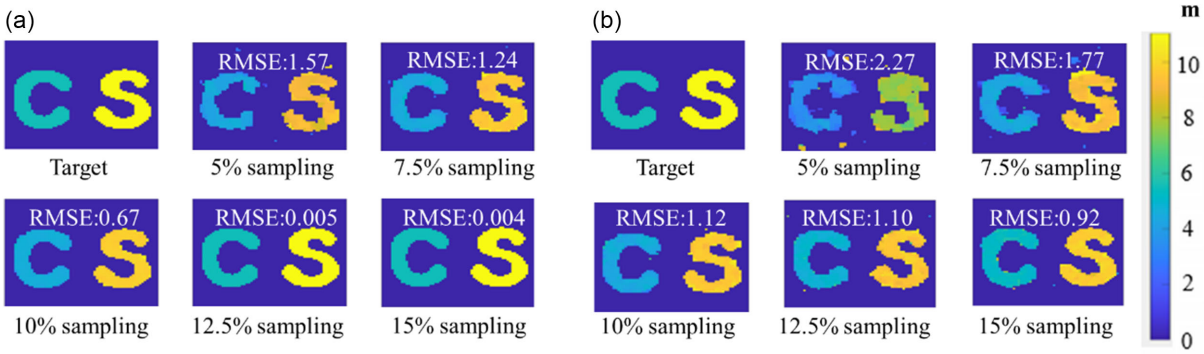

When the compression ratio is set at 5%, the RMSE for the reconstructed depth map measures at a mere 1.57. As we gradually increase the compression ratio, the RMSE of the reconstructed depth map consistently decreases. This decrease signifies that a greater number of measurements contribute to the refinement of depth map reconstruction. To gauge the robustness of our proposed system, we introduced 10 dB Gaussian white noise during our simulation experiments. The reconstruction results, depicted in Figure 3(b), unequivocally reveal the interference caused by noise during the depth map reconstruction process. In practical experiments, improving the accuracy of depth map reconstruction requires increasing the number of measurements (loading more observation matrices onto the DMD).

4. Experiments

The conceptual diagram of the compressive sensing-based coherent dual-frequency laser 3D imaging system is depicted in

Figure 4
Experimental system diagram

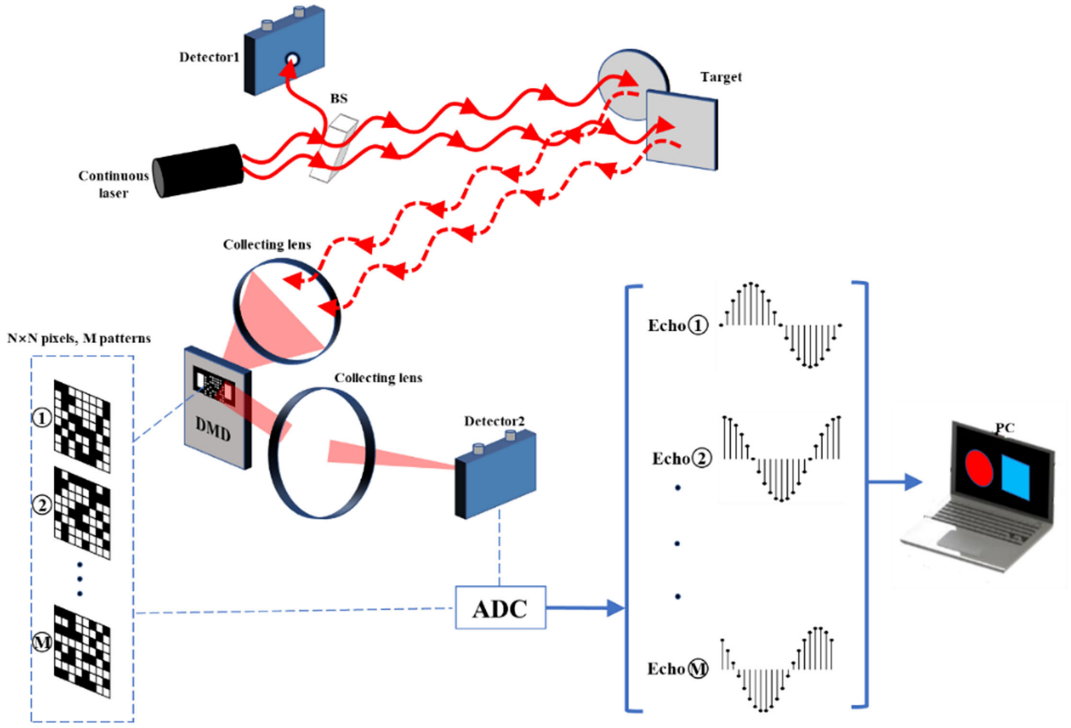

Figure 4. In this system, a coherent dual-frequency laser source, characterized by a frequency difference of 10 MHz, is employed to provide the necessary illumination. The emitted dual-frequency laser beam is ingeniously split into two distinct paths through the utilization of a beam splitter. One of these paths serves as the reference beam and is directly captured by photodetector 1, while the other path acts as the probing beam, illuminating the target object. Upon interaction with the target object, the light that is reflected undergoes further modulation, adding a layer of complexity to the process. This modulation is achieved by employing a DMD, which serves as a critical component of the system. After being focused by converging lens 1, the reflected light is directed toward the DMD. Here, the incident light waves interact with micromirrors that are in the "on" state, causing them to undergo reflection. These reflected light waves are then collected by photodetector 2, which, after being focused by converging lens 2, captures the modulated signal. It is noteworthy that the photodetectors employed in the experimental setup possess a bandwidth of 10 MHz and feature photosensitive surfaces with a substantial diameter of 2 mm. This choice of photodetectors with a large photosensitive surface diameter serves a dual purpose. Firstly, it enhances the efficiency of light signal collection, particularly crucial for the subsequent compressive sensing reconstruction. Secondly, it contributes to improved sensitivity and signal fidelity. Finally, the collected light signals, rich with information, undergo analog-to-digital conversion before being transmitted to a host computer for comprehensive signal processing and 3D reconstruction.

CS 3D imaging experiments were conducted on a variety of target shapes, including squares, circles, and triangles, positioned at a fixed distance of 1.35 m from the imaging system. To assess the impact of different sampling rates on the results, four distinct sampling rates, namely 0.2, 0.4, 0.6, and 0.8, were meticulously chosen for experimentation at 16 × 16 resolution. The findings of these experiments are thoughtfully presented in Figure 5.

The results unequivocally demonstrate a direct relationship between the system's sampling rate and the quality of 3D reconstructions, as measured by the RMSE of the reconstructed depth maps. As the sampling rate increases, the RMSE decreases, indicative of improved image recovery quality. Remarkably, at a high sampling rate of 0.8, the RMSE values for the 3D reconstruction of the different target shapes are notably reduced. Specifically, for the rectangular target, the RMSE stands at a mere 0.0856 m, while for the circular target, it is marginally higher at 0.0944 m. For the triangular target, the RMSE is slightly higher yet, at 0.1193 m.

The reconstructed target contours exhibit exceptional clarity, and intricate details are richly preserved. Among the various target shapes, the 3D imaging performance is notably superior for the rectangular target, followed closely by the circular target. This discrepancy in performance can be attributed to the inherent complexity of the target shapes and the implications for reconstruction. The rectangle, with its simpler contour, lends itself to more straightforward and accurate reconstruction, thus yielding the best results. In contrast, the triangular target, with fewer pixels representing its vertices, is more susceptible to the influence of surrounding noise points, which inevitably impacts its reconstruction quality, resulting in a comparatively poorer performance. In light of these findings, it is evident that future experiments should prioritize enhancing imaging resolution to bolster imaging accuracy.

We subsequently conducted CS-based 3D imaging experiments on square targets of varying sizes and distances, with an imaging resolution of 32 × 32. Three different square sizes (with side lengths of 2.5, 3, and 4 cm) and three different distances (1.7, 1.9, and 2.1 m) were utilized in the experiments. The experimental results, with a compression ratio of 0.25, are presented in Figure 6.

Figure 5
Compressed sensing 3D imaging results of a single target under different compression ratios

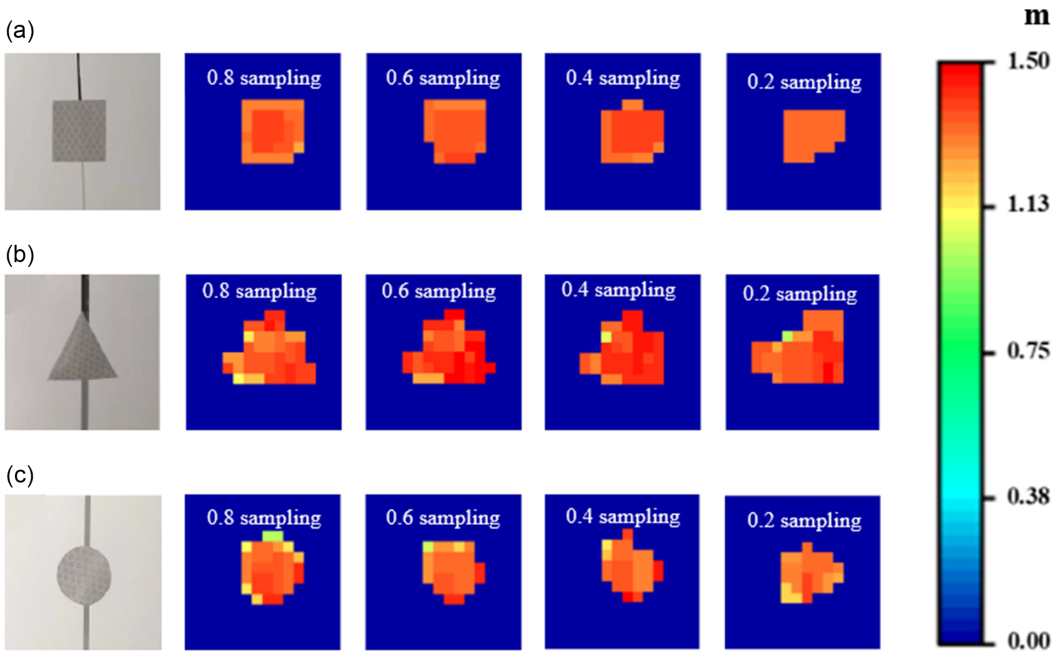

The experimental results demonstrate that the dual-frequency laser CS system can reconstruct depth maps with a minimal number of observations, achieving accurate shape and distance recovery. At a distance of 1.7 m, the reconstructed depths for three different-sized squares were 1.69, 1.73, and 1.64 m. At 1.9 m, the reconstructed depths for the same squares were 1.96, 1.93, and 1.90 m, while at 2.1 m, they were 2.16, 2.15, and 2.15 m. The average error in the reconstructed depth maps was approximately 0.037 m, with a maximum error of 0.06 m.

Furthermore, we also present in Figure 6 the number of pixels occupied by the reconstructed target depth maps. It is evident that, with a few exceptions, the number of pixels occupied by the reconstructed results increases with the target size and decreases with the distance. This observation aligns with practical expectations and confirms the accuracy of the reconstructed depth maps. This avenue of research holds the promise of advancing the state of the art in 3D imaging, particularly in scenarios involving intricate target geometries and noisy environments.

Figure 6
Results of compressed sensing 3D imaging of squares of different sizes at different distances. Distance1:1.7 m; distance2:1.9 m; distance3:2.1 m; square1: 2.5 cm; square2: 3 cm; square3: 4 cm

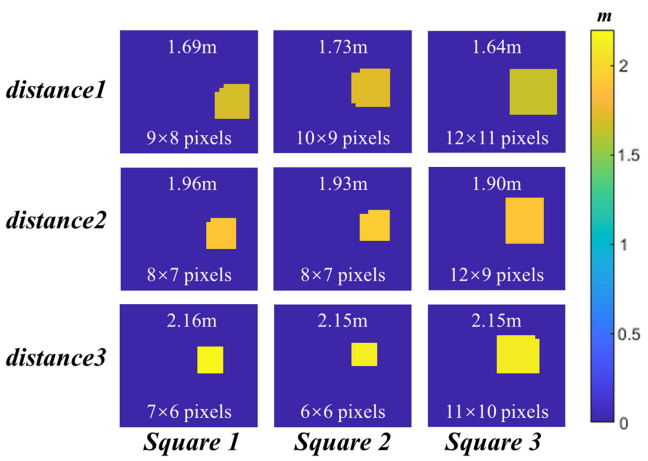

5. Conclusion

A CS-based coherent dual-frequency laser 3D imaging method is proposed. Compared to CS applied in pulsed lidar system, which requires multiple reconstruction calculations, the proposed method only requires two calculations to obtain the depth map of the target scene. Additionally, the CW detection system allows us to use more cost-effective, slow-speed square-law detectors while ensuring ranging accuracy. Simulation and experiments have confirmed that this method exhibits good ranging accuracy and interference resistance. The experiments successfully achieved compressed 3D imaging of different targets at a resolution of 16 × 16. The RMSE of the reconstructed depth maps at a 0.8 sampling rate was less than 0.12. Additionally, compressed 3D imaging at a resolution of 32 × 32 was performed on square targets of varying sizes and distances. The average depth error was approximately 0.037 m, with a maximum error of around 0.06 m. The next step involves using higher frequency difference coherent dual-frequency lasers and larger observation matrices to improve ranging accuracy and imaging resolution.

Funding Support

This work is supported by the Foundation of Key Laboratory of Lidar and Device, Sichuan Province, P.R. China (No.LLD2023-001).

Ethical Statement

This study does not contain any studies with human or animal subjects performed by any of the authors.

Conflicts of Interest

Zilong Zhang is an Editorial Board Member for *Journal of Optics and Photonics Research*, and was not involved in the editorial review or the decision to publish this article. The authors declare that they have no conflicts of interest to this work.

Data Availability Statement

Data available on request from the corresponding author upon reasonable request.

References

[1] Duarte, M. F., Davenport, M. A., Takhar, D., Laska, J. N., Sun, T., Kelly, K. F., & Baraniuk, R. G. (2008). Single-pixel imaging via compressive sampling. *IEEE Signal Processing Magazine*, *25*(2), 83–91. 10.1109/MSP.2007.914730

[2] Watts, C. M., Shrekenhamer, D., Montoya, J., Lipworth, G., Hunt, J., Sleasman, T., …, & Padilla, W. J. (2014). Terahertz compressive imaging with metamaterial spatial light modulators. *Nature Photonics*, *8*(8), 605–609. 10.1038/NPHOTON.2014.139

[3] Wang, L., & Zhao, S. (2021). Full color single pixel imaging by using multiple input single output technology. *Optics Express*, *29*(15), 24486–24499. 10.1364/OE.432864

[4] Wang, H., Bian, L., & Zhang, J. (2021). Depth acquisition in single-pixel imaging with multiplexed illumination. *Optics Express*, *29*(4), 4866–4874. 10.1364/OE.416481

[5] Álvarez, Y., Rodriguez-Vaqueiro, Y., Gonzalez-Valdes, B., Rappaport, C. M., Las-Heras, F., & Martínez-Lorenzo, J. Á. (2015). Three-dimensional compressed sensing-based millimeter-wave imaging. *IEEE Transactions on Antennas and Propagation*, *63*(12), 5868–5873. 10.1109/TAP.2015.2481487

[6] Li, F., Chen, H., Pediredla, A., Yeh, C., He, K., Veeraraghavan, A., & Cossairt, O. (2017). CS-ToF: High-resolution compressive time-of-flight imaging. *Optics Express*, *25*(25), 31096–31110. 10.1364/OE.25.031096

[7] Li, T., Dong, Y., & Wang, X. (2022). Fourier transform profilometry using single-pixel detection based on two-dimensional discrete cosine transform. *Optics & Laser Technology*, *156*, 108570. 10.1016/j.optlastec.2022.108570

[8] Zhang, Z., & Zhong, J. (2016). Three-dimensional single-pixel imaging with far fewer measurements than effective image pixels. *Optics Letters*, *41*(11), 2497–2500. 10.1364/OL.41.002497

[9] Zhang, Z., Liu, S., Peng, J., Yao, M., Zheng, G., & Zhong, J. (2018). Simultaneous spatial, spectral, and 3D compressive imaging via efficient Fourier single-pixel measurements. *Optica*, *5*(3), 315–319. 10.1364/OPTICA.5.000315

[10] Howland, G. A., Lum, D. J., Ware, M. R., & Howell, J. C. (2013). Photon counting compressive depth mapping. *Optics Express*, *21*(20), 23822–23837. 10.1364/OE.21.023822

[11] Li, S., Liu, X., Xiao, Y., Ma, Y., Yang, J., Zhu, K., & Tian, X. (2023). 3D compressive imaging system with a single photon-counting detector. *Optics Express*, *31*(3), 4712–4738. 10.1364/OE.473659

[12] Sun, M. J., Edgar, M. P., Gibson, G. M., Sun, B., Radwell, N., Lamb, R., & Padgett, M. J. (2016). Single-pixel three-dimensional imaging with time-based depth resolution. *Nature Communications*, *7*(1), 12010. 10.1038/ncomms12010

[13] Jie, Y., Li, X., Zhang, Z., Wang, J., Hu, Y., Li, Y., …, & Zhao, C. (2023). Three-dimensional imaging by compressed sensing based dual-frequency laser phase ranging. *APL Photonics*, *8*(7), 076104. 10.1063/5.0152561

[14] Kirmani, A., Colaço, A., Wong, F. N., & Goyal, V. K. (2011). Exploiting sparsity in time-of-flight range acquisition using a single time-resolved sensor. *Optics Express*, *19*(22), 21485–21507. 10.1364/OE.19.021485

[15] Liu, B., Song, P., Zhai, Y., Wang, X., & Zhang, W. (2021). Modeling and simulations of a three-dimensional ghost imaging method with differential correlation sampling. *Optics Express*, *29*(23), 38879–38893. 10.1364/OE.442889

[16] Lum, D. J., Knarr, S. H., & Howell, J. C. (2018). Frequency-modulated continuous-wave LiDAR compressive depth-mapping. *Optics Express*, *26*(12), 15420–15435. 10.1364/OE.26.015420

[17] Shi, G., Zheng, L., Wang, W., & Lu, K. (2020). Non-scanning three-dimensional imaging system with a single-pixel detector: Simulation and experimental study. *Applied Sciences*, *10*(9), 3100. 10.3390/app10093100

[18] Yang, Z., Bai, Y. M., Huang, K. X., Liu, Y. X., Liu, J., Ruan, D., & Li, J. L. (2023). Single-pixel full-field simultaneous spatial and velocity imaging. *Optics and Lasers in Engineering*, *169*, 107691. 10.1016/j.optlaseng.2023.107691

[19] Zhang, W., Cao, Z., Zhang, H., Xie, H., Ye, Z., & Xu, L. (2023). Distribution retrieval of both depth and reflectivity in 3-D objects via using modulated single pixel imaging. *IEEE Transactions on Instrumentation and Measurement*, *72*, 1–11. 10.1109/TIM.2022.3224515

[20] Li, Y., Xing, Y., Gao, Y., Zhang, H., Zhang, Z., & Zhao, C. (2021). A dual-frequency continuous wave doppler lidar for velocity measurement at far distance. *Microwave and Optical Technology Letters*, *63*(5), 1588–1594. 10.1002/mop.32797

[21] Cai, Y., Li, S., Zhang, W., Wu, H., Yao, X., & Zhao, Q. (2023). A detail-enhanced sampling strategy in Hadamard single-pixel imaging. *Chinese Optics Letters*, *21*(7), 071101. 10.3788/COL202321.071101

[22] Vaz, P. G., Amaral, D., Ferreira, L. R., Morgado, M., & Cardoso, J. (2020). Image quality of compressive single-pixel imaging using different Hadamard orderings. *Optics Express*, *28*(8), 11666–11681. 10.1364/OE.387612

[23] Yu, W. K., & Liu, Y. M. (2019). Single-pixel imaging with origami pattern construction. *Sensors*, *19*(23), 5135. 10.3390/s19235135

[24] Sun, M. J., Meng, L. T., Edgar, M. P., Padgett, M. J., & Radwell, N. (2017). A Russian Dolls ordering of the Hadamard basis for compressive single-pixel imaging. *Scientific Reports*, *7*(1), 3464. 10.1038/s41598-017-03725-6

[25] Yu, W. K. (2019). Super sub-Nyquist single-pixel imaging by means of cake-cutting Hadamard basis sort. *Sensors*, *19*(19), 4122. 10.3390/s19194122

How to Cite: Li, X., Hu, Y., Jie, Y., Zhao, C., & Zhang, Z. (2024). Dual-Frequency Lidar for Compressed Sensing 3D Imaging Based on All-Phase Fast Fourier Transform. *Journal of Optics and Photonics Research*, *1*(2), 74–81. https://doi.org/10.47852/bonviewJOPR32021565